MECSOL 2022 - Proceedings of the 8th International Symposium on Solid Mechanics
M.L. Bittencourt, J. Labaki, L.C.M. Vieira Jr. and E. Mesquita (Editors), Campinas SP, Brazil, October 17th to 19th, 2022

Aeroelastic Study of a Rotary-Wing using Non-linear Numerical Analysis

André Florentino Ribeiro[1], Murilo Sartorato[1] and Carlos do Carmo Pagani Junior[1]

[1]Universidade Estadual Paulista (UNESP). Av. Profa. Isette Correa Fontão, 505 - Jardim das Flores, São João da Boa Vista - SP, 13876-750

Abstract. Rotary-wings aeroelasticity is a field widely studied in order to improve the accuracy of fluid-structure interaction responses using low computational effort. These aeroelastic analyses demand integrated models for both the structural and the aerodynamical theories to properly describe the behavior of a rotary-wing. This work proposes the implementation of a semi-aeroelastic numerical model that uses a mixed variational finite element theory to analyze the aeroelastic behavior of a rotary-wing at hovering flight. The structural model stems from the Variational Asymptotic Method (VAM) and relies on the Variation Beam Section Analysis (VABS) to be capable of modeling composite material structures as geometrically non-linear beams. Also, the aerodynamic model, which computes the driving distributed loads on the structure, is based on the thin airfoil theory and predicts the rotor aerodynamic field which will import the steady-state induced velocity of the blade from a Blade Element Moment Theory (BEMT) analysis using an interaction process. For the purpose of assembling the distributed aerodynamic load in the finite element structural model, the distributed load will be transformed into concentrated equivalent loads in each element node using the numerical integration Gauss Quadrature Method. Furthermore, the Newton-Raphson Method is applied to numerically solve the non-linear equations for obtaining the steady-state response of a wing along the aerodynamic field in terms of geometric parameters, material properties, rotary speed and aerodinamic coefficients. This formulation will be used to describe the aeroelastic behavior of a rotary-wing mainly made of carbon-epoxy laminate and aramid fiber honeycomb composite materials that has the UH-60A airfoil as cross-section. The results will present the steady aerodynamic forces distribution, the internal efforts and blade's displacements. Preliminary results show that the tip loss of the lift and drag starts in about 93% of the length of the blade, and that the axial force is the critical force acting on the rotor

Keywords: Finite Element Method, Fluid-structure interaction, Non-linear analysis, Rotary Blades, Composite Materials

INTRODUCTION

Rotary-wings aeroelasticity is a field widely studied in order to improve the accuracy of fluid-structure responses, and it needs to integrate both structural and aerodynamics theories to be properly described. Nowadays, since most of the rotary blades are build in composite materials, the structural model needs to be capable of predicting all the internals stresses and deformations of these type of materials. Also, the aerodynamic model needs to compute the distributed loads applied on the blade, which can be a function of the deformations (Shang, 1995).

Modern helicopter blades usually have high aspect ratios, so it is acceeptable to model them using beam theories, although their high flexibility and range operation lead to non-linear behavior (Hodges, 2006). Composite materials are also widely used in the constructions of blades duo to their good fatigue life, high strain-to-weight ratio and low maintenance costs (Ghorashi, 2016). But it can be a challenge to structurally model composite materials due to the anisotropic behavior that involves the coupling among the extension, bending, torsion and shear deformations.

The Variational Asymptotic Method (VAM), in addition to Variation Asymptotic Beam Section (VABS) are effective numerical techniques used to model composite blades as beams. The VAM divides a 3D structural analysis in two complementary formulations: a main 1D geometrically nonlinear analysis discretized by finite element method (FEM) that follows the beam reference line; and a 2D linear analysis which predicts the effect of each element cross-section using VABS. This method yields results with a high level of accuracy, in spite of a strong reduction in the number of degrees of freedom required by to build a 3D finite elements analysis (Hodges, 1990).

Helicopter rotor's aerodynamic theories are used to compute the spanwise lift force, drag force and pitch moment for an airfoil that performs a sinusoidal movement. The aerodynamic load applied on the blade is proportional to the current blade's elastic deformations, which integrates both the structural and aerodynamic models into an aeroelastic one. So, this work studies the aeroelastic behavior response of a helicopter blade fully manufactured with composite material which uses the UH-60A airfoil as cross-section. It is important to note that the assumption of steady induced flow, here derived

from the BEMT, leads to a simplified aeroelastic model which, according to Hodges and Ormiston (1976), is judge to be suitable for the stability analysis of blades flapping at low frequencies in hovering flight.

ROTARY BLADE AEROELASTIC FORMULATION

The rotary blade aeroelastic formulation is mainly based on a mixed variational formulation finite elements method (FEM) with a one-dimensional discretized clamped-free beam. The nodal loads are computed using an aeroelastic model with numerical integration along the element's length, while the internal energy equilibrium is formulated using geometrically non-linear Langragean beams (Shang, 1995).

References Frames

The nonlinear beam representation requires three different references frames. As shown in Fig. (1), these systems are: 1) global frame (a_1, a_2, a_3) that rotates along the rotor and is defined by the rotor's rotation plane; 2) non-deformed beam frame (b_1, b_2, b_3) that is used to identify every beam's element initial condition; and 3) deformed beam frame (B_1, B_2, B_3) that is used to represent every beam's element orientation on the deformed state.

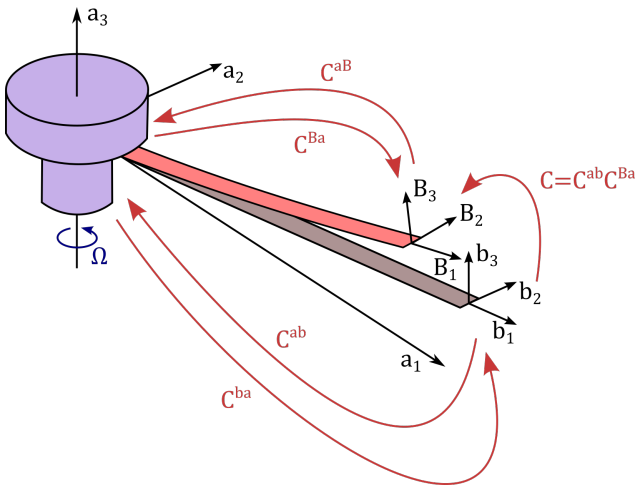

Figure 1: The global frame a_i rotates with the rotor. The reference frame b_i represents the non-deformed beam state. The reference frame B_i represents the deformed beam state

The linear and angular displacements vectors $\mathbf{u}$ and $\boldsymbol{\theta}$, respectively, are measured on the global frame a_i. However, the deformation $\boldsymbol{\gamma}$, curvature $\boldsymbol{\kappa}$, linear speed $\boldsymbol{V}$, angular speed $\boldsymbol{\Omega}$, linear momentum $\mathbf{P}$, angular momentum $\mathbf{H}$, internal force $\mathbf{F}$ and internal moment $\mathbf{M}$ vectors are measured on the deformed frame B_i (Cheng, 2002). Even though the internal forces and moments are measured on the beam's deformed state B_i, the static equilibrium condition is calculated on the beam's undeformed state b_i as per a Lagrangean equilibrium definition (Ghorashi, 2016).

The use of the reference coordinate systems previously mentioned requires the usage of coordinate transformation matrices. These matrices are following listed:

- $\mathbf{C}^{ba}$: transformation matrix from coordinate system a_i to b_i;
- $\mathbf{C}^{ab}$: transformation matrix from coordinate system b_i to a_i;
- $\mathbf{C}^{aB}$: transformation matrix from coordinate system B_i to a_i;
- $\mathbf{C}^{Ba}$: transformation matrix from coordinate system a_i to B_i.

For untwisted blades, the transformation matrices, $\mathbf{C}^{ba}$ and $\mathbf{C}^{ab}$, are functions of the collective pitch angle θ_{pitch} written as

$$\mathbf{C}^{ba}(\theta_{pitch}) = \begin{bmatrix} 1 & 0 & 0 \\ 0 & cos(\theta_{pitch}) & sin(\theta_{pitch}) \\ 0 & -sin(\theta_{pitch}) & cos(\theta_{pitch}) \end{bmatrix} \tag{1}$$

$$\mathbf{C}^{ab} = \mathbf{C}^{ba^T} \tag{2}$$

Also, the rotation matrix, $\mathbf{C}$, can be obtained by Eq. (3).

$$\mathbf{C} = \mathbf{C}^{ab}\mathbf{C}^{Ba} \tag{3}$$

So, the rotation matrix can be written in function of the angular displacements $\boldsymbol{\theta}$, as shown in Eq. (4).

$$\mathbf{C}(\boldsymbol{\theta}) = \frac{\left(1 - \frac{\boldsymbol{\theta}^T\boldsymbol{\theta}}{4}\right)\boldsymbol{\Delta} - \tilde{\boldsymbol{\theta}} + \frac{\boldsymbol{\theta}^T\boldsymbol{\theta}}{2}}{1 + \frac{\boldsymbol{\theta}^T\boldsymbol{\theta}}{4}} \tag{4}$$

The angular displacements $\boldsymbol{\theta}$ are the rotation vector set as a parametrization of the nodal rotation magnitude in terms of Rodrigues' Parameters (Hodges, 2006). Also, the operator $\tilde{()}$ transform a vector to its dual matrix, that is, if $\boldsymbol{e} = [e_1\ e_2\ e_3]^T$ so

$$\tilde{\boldsymbol{e}} = \begin{bmatrix} 0 & -e_3 & e_2 \\ e_3 & 0 & -e_1 \\ -e_2 & e_1 & 0 \end{bmatrix} \tag{5}$$

Aerodynamic Model

Andrade (1992) used a aerodynamic theory based on the thin airfoil to describe the spanwise aerodynamic load which stems from a generalized Theodorsen theory proposed by Greenberg (Hodges and Ormiston, 1976). This theory is applied on airfoils that performs a sinusoidal movement, on which the air flow around the airfoil can be expressed with two components: 1) circulatory, that is, associated with the wake vortex developed at the trialling edge; 2) non-circulatory, associated with the downwash inflow which yields inertial forces because of the mass movement.

Figure (2) shows the aerodynamic loads acting on the airfoil, where $\vec{L}_C$ is the circulatory lift, $\vec{L}_{NC}$ is the non-circulatory lift, $\vec{D}$ is the sum between the induced drag and the profile drag and $\vec{M}$ is the sum between the circulatory and the non-circulatory pitch moments.

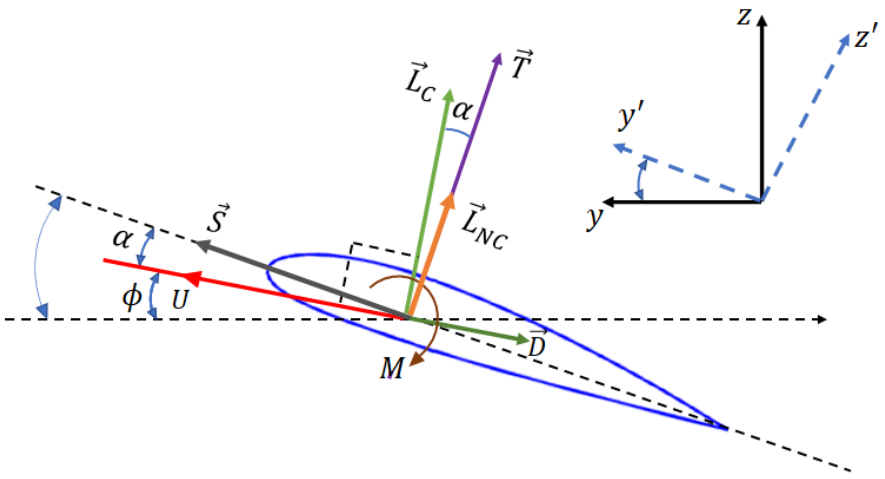

Figure 2: Representation of circulatory and non-circulatory forces acting on the airfoil

In the mixed variational beam formulation, Eq. (6) and (7) represents the steady aerodynamic loads in the B_i frame expressed as distributed loads.

$$\mathbf{f}_B = \frac{1}{2} ac\rho_\infty \left\{ \begin{array}{c} 0 \\ \left(U_P - \frac{c}{2}\Omega_1\right) U_P - \frac{c_{d_0}}{2} U_T^2 \\ \left(\frac{c}{2}\Omega_1 - U_P\right) U_T. \end{array} \right\} \tag{6}$$

$$\mathbf{m}_B = -\frac{1}{32}\rho_\infty a c^3 \left\{ \begin{array}{c} U_T \Omega_1 \\ 0 \\ 0 \end{array} \right\} \tag{7}$$

where ρ is the mass density of air, c is the chord length, a is the lift curve slope, c_{d_0} is the profile drag coefficient, U_T and U_P are the relative velocity components, parallel and normal to the airfoil line in B_i frame respectively, defined as:

$$U_T = \mathbf{e}_2^T \left(\mathbf{V}_B + \mathbf{C}^{ba} \mathbf{C} \lambda \mathbf{e}_3 \right) \tag{8}$$

$$U_P = \mathbf{e}_3^T \left(\mathbf{V}_B + \mathbf{C}^{ba} \mathbf{C} \lambda \mathbf{e}_3 \right), \tag{9}$$

In Eq. (8) and (9), λ is the wake-induced inflow velocity which is included explicitly in the angle of attack and $\mathbf{V_B}$ is the inertial velocity in the aerodynamic center of the airfoil represented as

$$\mathbf{V}_B = \mathbf{C}^{Ba} \left[\mathbf{v}_a + \dot{\mathbf{u}}_a + \widetilde{\omega}_a \left(\mathbf{u}_a + \mathbf{d} \right) \right], \tag{10}$$

The aerodynamic force and moments are transformed into the global coordinate system a_i as

$$\begin{array}{r} \mathbf{f}_a = \mathbf{C}^T \mathbf{C}^{ab} \mathbf{f}_B \\ \mathbf{m}_a = \mathbf{C}^T \mathbf{C}^{ab} \mathbf{m}_B \end{array} \tag{11}$$

where $\mathbf{u}_a$ is the linear displacements caused by deformation, $\mathbf{v}_a$ is the rotor's linear velocity and $\boldsymbol{\omega}_a$ is the rotor's angular velocity. The wake-induced inflow λ will calculated using Blade Element Moment Theory (BEMT) and incorporated to this model.

Structural Model

Cross-Sectional Bi-dimensional Energy Analysis

The VAM involves bi-dimensional analyses, which are made by establishing structural parameters from kinetic energy, deformation energy and work of external efforts. The energy equations requires generalized 6x6 matrices that describes the cross-section stiffness and inertia behavior and are obtained by taking into account the shape of the the section and its material proprieties distributions (Cesnik, 1994). In most of the cases, VABS is used to compute this matrices.

In beams made of composite materials that has the displacements and curvature coupled, the cross-sectional stiffness matrix $\mathbf{S}$ is a 6x6 matrix entirely populated. In that case, the constitutive material equation that associate forces $\mathbf{F}$ and moments $\mathbf{M}$ with the deformations $\boldsymbol{\gamma}$ and curvatures $\boldsymbol{\kappa}$, is written as:

$$\left\{ \begin{array}{c} F_1 \\ F_2 \\ F_3 \\ M_1 \\ M_2 \\ M_3 \end{array} \right\} = \left[\begin{array}{cccccc} S_{11} & S_{12} & S_{13} & S_{14} & S_{15} & S_{16} \\ S_{21} & S_{22} & S_{23} & S_{24} & S_{25} & S_{26} \\ S_{31} & S_{32} & S_{33} & S_{34} & S_{35} & S_{36} \\ S_{41} & S_{42} & S_{43} & S_{44} & S_{45} & S_{46} \\ S_{51} & S_{52} & S_{53} & S_{54} & S_{55} & S_{56} \\ S_{61} & S_{62} & S_{63} & S_{64} & S_{65} & S_{66} \end{array} \right] \left\{ \begin{array}{c} \gamma_{11} \\ 2\gamma_{12} \\ 2\gamma_{13} \\ \kappa_1 \\ \kappa_2 \\ \kappa_3 \end{array} \right\} \tag{12}$$

The deformation energy density for the beam's cross-section, U, can be calculated from:

$$\mathscr{U} = \frac{1}{2} \left\{ \begin{array}{c} \boldsymbol{\gamma} \\ \boldsymbol{\kappa} \end{array} \right\}^T \left[\begin{array}{cc} \mathbf{A}_{3x3} & \mathbf{B}_{3x3} \\ \mathbf{B}^T & \mathbf{D}_{3x3} \end{array} \right] \left\{ \begin{array}{c} \boldsymbol{\gamma} \\ \boldsymbol{\kappa} \end{array} \right\} \tag{13}$$

where **A** has the force stiffness terms, **B** has the curvature-force related stiffness terms, and **D** has the moment stiffness terms.

The linear and angular momentum of the beam are obtained by relating the linear and angular speed with a cross-sectional inertia matrix that represents the inertia of the beam per length unit. The vectors $\mathbf{P}_B$, $\mathbf{H}_B$, $\mathbf{V}_B$, $\mathbf{\Omega}_B$, which are the linear momentum, angular momentum, linear velocity, and angular velocity, respectively, have the "B" subscript because they are measured on the deformed beam coordinate system B_i (see Fig. 1).

The relation of $\mathbf{P}_B$ and $\mathbf{H}_B$ with $\mathbf{V}_B$ and $\mathbf{\Omega}_B$ are expressed as:

$$\left\{ \begin{array}{c} \mathbf{P}_B \\ \mathbf{H}_B \end{array} \right\} = [\mathbf{I}] \left\{ \begin{array}{c} \mathbf{V}_B \\ \mathbf{\Omega}_B \end{array} \right\} \tag{14}$$

$$\left\{ \begin{array}{c} P_1 \\ P_2 \\ P_3 \\ H_1 \\ H_2 \\ H_3 \end{array} \right\} = \left[\begin{array}{cccccc} \mu & 0 & 0 & 0 & \mu\bar{x}_3 & -\mu\bar{x}_2 \\ 0 & \mu & 0 & -\mu\bar{x}_3 & 0 & 0 \\ 0 & 0 & \mu & \mu\bar{x}_2 & 0 & 0 \\ 0 & -\mu\bar{x}_3 & \mu\bar{x}_2 & i_2+i_3 & 0 & 0 \\ \mu\bar{x}_3 & 0 & 0 & 0 & i_2 & i_{23} \\ -\mu\bar{x}_2 & 0 & 0 & 0 & i_{23} & i_3 \end{array} \right] \left\{ \begin{array}{c} V_1 \\ V_2 \\ V_3 \\ \Omega_1 \\ \Omega_2 \\ \Omega_3 \end{array} \right\} \tag{15}$$

where μ is the mass density per unit length, $\bar{x}_2$ and $\bar{x}_3$ are the distances of the center of mass and the shear center of the cross-section, i_2 and i_3 are the mass moments per unit length in the a_2 and a_3 directions, and i_{23} is the product of inertia per unit length.

Also, the kinetic energy for the beam's cross-section, K, can be obtained as following:

$$\mathscr{K} = \frac{1}{2} \left\{ \begin{array}{c} \mathbf{V}_B \\ \mathbf{\Omega}_B \end{array} \right\}^T \left[\begin{array}{cc} \mu\mathbf{\Delta} & -\mu\bar{\bar{\boldsymbol{\xi}}} \\ \mu\bar{\bar{\boldsymbol{\xi}}} & \mathbf{i} \end{array} \right] \left\{ \begin{array}{c} \mathbf{V}_B \\ \mathbf{\Omega}_B \end{array} \right\} \tag{16}$$

Variational Formulation and Finite Elements Discretization

The variational formulation which stands for the rotary beam equations is based on the Hamilton's principle (cite CHENG)

$$\int_{t_1}^{t_2} \int_0^l \left[\delta(\mathscr{K} - \mathscr{U}) + \delta\bar{W} \right] dx_1 dt = \delta\bar{A} \tag{17}$$

where t_1 and t_2 are arbitrary times, l is the length of the beam, $\mathscr{K}$ and $\mathscr{U}$ are the kinetic and deformation energy density per unit length, respectively, $\delta\bar{W}$ is the virtual work of external loads on the system per unit length, and $\delta\bar{A}$ is the virtual action of the conservative aerodynamic forces between t_1 and t_2.

The virtual variation of the kinetic energy stems from the variation of the vectors $\mathbf{V_B}$ and $\mathbf{\Omega_B}$, and the virtual variation of the potential energy stems from the variation of the vectors $\boldsymbol{\gamma}$ and $\boldsymbol{\kappa}$. Also, the nonlinear equations derived from the application of Hamilton's principle (Eq. (17)) are discretized for finite elements applications with 18 degrees of freedom per node. The degrees of freedom are contained in the following vectors: linear displacements **u**, angular displacements $\boldsymbol{\theta}$, force **F**, moment **M**, linear momentum **P** and angular momentum **H**. Since a node has both displacements and loads as degrees of freedom, the elements is described by a mixed formulation.

This finite element model is proposed by Shang (1995) and comes from the integration of Eq. (17) within each element which provides the equations starting from Eq. (18) up to Eq. (27), where the subscript i term indicates the i^{th} element and f are the internal force related to the degree of freedom of the subscript index.

$$\boldsymbol{f}_{u_i} = -\mathbf{C}^T\mathbf{C}^{ab}\mathbf{F}_i + \frac{\Delta l_i}{2}\tilde{\boldsymbol{\omega}}_a\mathbf{C}^T\mathbf{C}^{ab}\mathbf{P}_i + \frac{\Delta l_i}{2}\left(\mathbf{C}^T\mathbf{C}^{ab}\mathbf{P}_i\right)^* - \bar{\mathbf{f}}_i \tag{18}$$

$$\boldsymbol{f}_{\psi_i} = -\mathbf{C}^T\mathbf{C}^{ab}\mathbf{M}_i + \frac{\Delta l_i}{2}\mathbf{C}^T\mathbf{C}^{ab}\left(\tilde{\boldsymbol{e}}_1 + \tilde{\boldsymbol{\gamma}}_i\right)\mathbf{F}_i + \frac{\Delta l_i}{2}\left(\tilde{\boldsymbol{\omega}}_a\mathbf{C}^T\mathbf{C}^{ab}\mathbf{H}_i + \mathbf{C}^T\mathbf{C}^{ab}\tilde{\mathbf{V}}_i\mathbf{P}_i\right) + \frac{\Delta l_i}{2}\left(\mathbf{C}^T\mathbf{C}^{ab}\mathbf{H}_i\right)^* - \bar{\mathbf{m}}_i \tag{19}$$

$$\boldsymbol{f}_{F_i} = \mathbf{u}_i - \frac{\Delta l_i}{2}\left[\mathbf{C}^T\mathbf{C}^{ab}\left(\boldsymbol{e}_1+\boldsymbol{\gamma}_i\right) - \mathbf{C}^{ab}\boldsymbol{e}_1\right] \tag{20}$$

$$\boldsymbol{f}_{M_i} = \boldsymbol{\theta}_i - \frac{\Delta l_i}{2}\left[\boldsymbol{\Delta} + \frac{\tilde{\boldsymbol{\theta}}_i}{2} + \frac{\boldsymbol{\theta}_i\boldsymbol{\theta}_i^T}{4}\right]\mathbf{C}^{ab}\boldsymbol{\kappa}_i \tag{21}$$

$$\boldsymbol{f}_{P_i} = \mathbf{C}^T\mathbf{C}^{ab}\mathbf{V}_i - \boldsymbol{v}_a - \tilde{\boldsymbol{\omega}}_a\left(\mathbf{u}_i + D_{l_i}\right) - \dot{\mathbf{u}}_i \tag{22}$$

$$\boldsymbol{f}_{H_i} = \boldsymbol{\Omega}_i - \mathbf{C}^{ba}\mathbf{C}\boldsymbol{\omega}_a - \mathbf{C}^{ba}\left(\frac{\boldsymbol{\Delta} - \tilde{\boldsymbol{\theta}}_i/2}{1+\boldsymbol{\theta}_i^T\boldsymbol{\theta}_i/4}\right)\dot{\boldsymbol{\theta}}_i \tag{23}$$

$$\boldsymbol{f}_{u_{i+1}} = \mathbf{C}^T\mathbf{C}^{ab}\mathbf{F}_i + \frac{\Delta l_i}{2}\tilde{\boldsymbol{\omega}}_a\mathbf{C}^T\mathbf{C}^{ab}\mathbf{P}_i + \frac{\Delta l_i}{2}\left(\mathbf{C}^T\mathbf{C}^{ab}\mathbf{P}_i\right)^* - \bar{\mathbf{f}}_{i+1} \tag{24}$$

$$\boldsymbol{f}_{\psi_{i+1}} = \mathbf{C}^T\mathbf{C}^{ab}\mathbf{M}_i + \frac{\Delta l_i}{2}\mathbf{C}^T\mathbf{C}^{ab}\left(\tilde{\boldsymbol{e}}_1+\tilde{\boldsymbol{\gamma}}_i\right)\mathbf{F}_i + \frac{\Delta l_i}{2}\left(\tilde{\boldsymbol{\omega}}_a\mathbf{C}^T\mathbf{C}^{ab}\mathbf{H}_i + \mathbf{C}^T\mathbf{C}^{ab}\tilde{\mathbf{V}}_i\mathbf{P}_i\right) + \frac{\Delta l_i}{2}\left(\mathbf{C}^T\mathbf{C}^{ab}\mathbf{H}_i\right)^* - \bar{\mathbf{m}}_{i+1} \tag{25}$$

$$\boldsymbol{f}_{F_{i+1}} = -\mathbf{u}_i - \frac{\Delta l_i}{2}\left[\mathbf{C}^T\mathbf{C}^{ab}\left(\boldsymbol{e}_1+\boldsymbol{\gamma}_i\right) - \mathbf{C}^{ab}\boldsymbol{e}_1\right] \tag{26}$$

$$\boldsymbol{f}_{M_{i+1}} = -\boldsymbol{\theta}_i - \frac{\Delta l_i}{2}\left[\boldsymbol{\Delta} + \frac{\tilde{\boldsymbol{\theta}}_i}{2} + \frac{\boldsymbol{\theta}_i\boldsymbol{\theta}_i^T}{4}\right]\mathbf{C}^{ab}\boldsymbol{\kappa}_i \tag{27}$$

In the equations above, the effective nodal loads are obtained by Gauss Quadrature numerical integration:

$$\begin{array}{ll} \bar{\mathbf{f}}_i = \int_{l_i}(1-\xi)\,\mathbf{f}_a dx_1 & \bar{\mathbf{f}}_{i+1} = \int_{l_i}\xi\mathbf{f}_a dx_1 \\ \bar{\mathbf{m}}_i = \int_{l_i}(1-\xi)\,\mathbf{m}_a dx_1 & \bar{\mathbf{m}}_{i+1} = \int_{l_i}\xi\mathbf{m}_a dx_1 \end{array} \tag{28}$$

Since the blade is unique and has all elements aligned in one direction, and each j^{th} node with $j \neq 1, N+1$ belongs to two sequenced elements, the global matrix with N elements is assembled as Eq. (29) and Eq. (30) , while $\mathbf{F_S}$ is the structure operator and $\mathbf{F_L}$ is the load operator.

$$\begin{aligned}\mathbf{F_S} = [&\boldsymbol{f}_{u_1}^{(1)} + \hat{\mathbf{F}}_0 \quad \boldsymbol{f}_{\psi_1}^{(1)} + \hat{\mathbf{M}}_0 \quad \boldsymbol{f}_{F_1}^{(1)} \quad \boldsymbol{f}_{M_1}^{(1)} \quad \boldsymbol{f}_{P_1}^{(1)} \quad \boldsymbol{f}_{H_1}^{(1)} \quad \boldsymbol{f}_{u_2}^{(1)} + \boldsymbol{f}_{u_2}^{(2)} \quad \boldsymbol{f}_{\psi_2}^{(1)} + \boldsymbol{f}_{\psi_2}^{(2)} \quad \boldsymbol{f}_{F_2}^{(1)} + \boldsymbol{f}_{F_2}^{(2)} \quad \boldsymbol{f}_{M_2}^{(1)} + \boldsymbol{f}_{M_2}^{(2)} \\ &\cdots \quad \boldsymbol{f}_{F_i}^{(i)} \quad \boldsymbol{f}_{M_i}^{(i)} \quad \boldsymbol{f}_{P_i}^{(i)} \quad \boldsymbol{f}_{H_i}^{(i)} \quad \boldsymbol{f}_{u_{i+1}}^{(i)} + \boldsymbol{f}_{u_{i-1}}^{(i+1)} \quad \boldsymbol{f}_{\psi_{i+1}}^{(i)} + \boldsymbol{f}_{\psi_{i+1}}^{(i+1)} \quad \boldsymbol{f}_{F_{i+1}}^{(i)} + \boldsymbol{f}_{F_{i+1}}^{(i+1)} \quad \boldsymbol{f}_{M_{i+1}}^{(i)} + \boldsymbol{f}_{M_{i+1}}^{(i+1)} \quad \cdots \\ &\qquad\qquad\qquad\qquad\qquad\qquad\qquad\qquad\qquad\qquad\qquad\qquad \boldsymbol{f}_{u_N}^{(N)} \quad \boldsymbol{f}_{\psi_N}^{(N)} \quad \boldsymbol{f}_{F_N}^{(N)} + \hat{\boldsymbol{u}}_{N+1} \quad \boldsymbol{f}_{M_N}^{(N)} + \hat{\boldsymbol{\theta}}_{N+1}]^T\end{aligned} \tag{29}$$

$$\begin{aligned}\mathbf{F_L} = [&\bar{\mathbf{f}}_1^{(1)} \quad \bar{\mathbf{m}}_1^{(1)} \quad 0 \quad 0 \quad 0 \quad 0 \quad \bar{\mathbf{f}}_2^{(1)} + \bar{\mathbf{f}}_2^{(2)} \quad \bar{\mathbf{m}}_2^{(1)} + \bar{\mathbf{m}}_2^{(2)} \quad \cdots \quad \bar{\mathbf{f}}_i^{(i)} \quad \bar{\mathbf{m}}_i^{(i)} \quad 0 \quad 0 \quad 0 \quad 0 \quad \bar{\mathbf{f}}_{i+1}^{(i)} + \bar{\mathbf{f}}_{i+1}^{(i+1)} \\ &\qquad\qquad\qquad\qquad\qquad\qquad\qquad\qquad\qquad\qquad\qquad\qquad \bar{\mathbf{m}}_{i+1}^{(i)} + \bar{\mathbf{m}}_{i+1}^{(i+1)} \quad \cdots \quad \bar{\mathbf{f}}_{N+1}^{(N)} \quad \bar{\mathbf{m}}_{N+1}^{(N)} \quad 0 \quad 0]^T\end{aligned} \tag{30}$$

In Eq. (29) and Eq. (30), the superscript indicates the element number and the subscript the node number. The two previous equations lead to the solution variable $\mathbf{X}$ that depends on the boundary conditions

$$\mathbf{X} = [\mathbf{X}_{root} \quad \mathbf{X}_{common} \quad \mathbf{X}_{tip}]^T \tag{31}$$

The hingeless helicopter blade is treated as a clamped-free beam, so, assuming that the $\mathbf{X}_{common}$ vector represents all the middle nodes that have all degrees of freedom, the solution vector is

$$\mathbf{X} = [\hat{\mathbf{F}}_0 \quad \hat{\mathbf{M}}_0 \quad \mathbf{u}_1 \quad \boldsymbol{\theta}_1 \quad \mathbf{F}_1 \quad \mathbf{M}_1 \quad \mathbf{P}_1 \quad \mathbf{H}_1 \quad \dots \quad \mathbf{u}_N \quad \boldsymbol{\theta}_N \quad \mathbf{F}_N \quad \mathbf{M}_N \quad \mathbf{P}_N \quad \mathbf{H}_N \quad \hat{\mathbf{u}}_{N+1} \quad \hat{\boldsymbol{\theta}}_{N+1}]^T \tag{32}$$

Therefore, the nonlinear equation, in steady-state, that need to be solved is

$$\mathbf{F}(\mathbf{X}) = \mathbf{F_S}(\mathbf{X}) - \mathbf{F_L}(\mathbf{X}) = 0 \tag{33}$$

Equation. (33) is solved by Newton-Raphson method with increment k iteration

$$\mathbf{J}(\mathbf{X^k})\Delta\mathbf{X^k} = -\mathbf{F}(\mathbf{X^k}) \tag{34}$$

$$\mathbf{X^{k+1}} = \mathbf{X^k} + \Delta\mathbf{X^k} \tag{35}$$

where $\mathbf{J}(\mathbf{X})$ is the Jacobian matrix analytically calculated defined as

$$\mathbf{J}(\mathbf{X}) = \frac{\partial \mathbf{F_S}(\mathbf{X})}{\partial \mathbf{X}} - \frac{\partial \mathbf{F_L}(\mathbf{X})}{\partial \mathbf{X}} \tag{36}$$

SIMULATION SETUP

The simulated blade consists in a rectangular blade with the UH60A as cross-sectional shape. The cross-section is mainly made by Plascore honeycomb and has a box-spar made by Carbon Fiber laminate with Aluminum 8009 in the leading edge surface. VABS (Tian et al., 2021) (Atilgan and Hodges, 1991) has been run in the section, and Fig. (3) presents its mesh. The output results are the 6x6 Timoshenko matrices shown in Eqs. (37) and (38).

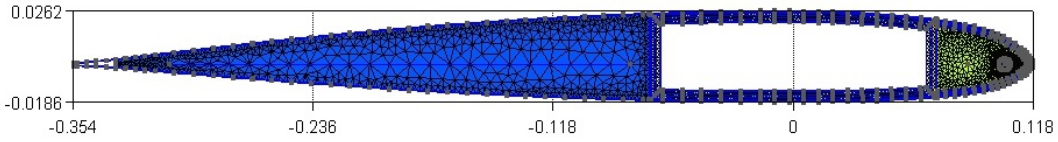

Figure 3: Cross-sectional VABS Mesh

$$\mathbf{S} = \begin{bmatrix} 2722 & 0.03555 & 0.02767 & 0.1773 & 8.8478 & -42.84 \\ 0.3555 & 903.6 & -8.1554 & -3.8010 & -0.1151 & 0.006190 \\ 0.02767 & -8.1554 & 129.54 & 1.9401 & 0.003477 & 0.1675 \\ 0.1773 & -3.8010 & 1.9401 & 1.1338 & 0.0009266 & -0.004962 \\ 8.8478 & -0.1151 & 0.003477 & 0.0009266 & 0.8470 & -0.05198 \\ -42.84 & 0.0061901 & 0.1675 & -0.004962 & -0.05198 & 10.59 \end{bmatrix} \times 10^3 \tag{37}$$

$$\mathbf{I} = \begin{bmatrix} 1.1360 \times 10^{-2} & 0 & 0 & 0 & 0 & 0 \\ 0 & 1.1360 \times 10^{-2} & 0 & 0 & 0 & 0 \\ 0 & 0 & 1.1360 \times 10^{-2} & 0 & 0 & 0 \\ 0 & 0 & 0 & 1.3624 \times 10^{-4} & 0 & 0 \\ 0 & 0 & 0 & 0 & 2.832 \times 10^{-6} & 4.0748 \times 10^{-8} \\ 0 & 0 & 0 & 0 & 4.0748 \times 10^{-8} & 1.3341 \times 10^{-4} \end{bmatrix} \tag{38}$$

The units associated with the stiffness values are S_{ij} $[N]$, $S_{i,j+3}$ $[N.m]$, and $S_{i+3,j+3}$ $[N.m^2]$. Also, this cross-section is used to build the rotor that has the properties described in the Tab. (1). The rotor is used to simulate a hover flight ($\mathbf{v}_a = [0\ 0\ 0]^T$) with the roll, pitch and yaw angles are zero.

Table 1: Characteristics of the Rotor

Variable	Description	Value
e	root cutoff	$0.2\ m$
l	rotor length	$2.0\ m$
c	chord length	$0.472\ m$
ρ	air density	$1.225\ kg/m^3$
ω_{a_3}	rotor speed	$250\ RPM$
a	lift-curve slope	6.390
C_{d_0}	profile drag	0.00508
Q	number of blades	2
θ_{pitch}	pitch angle	$8°$

RESULTS

The number of elements used was 13, as used by Shang (1995). The steady-state response of the rotor for each blade are shown in Figs. (4-6), where:

Lift, induced drag and moment and inflow distributions: Fig. (4);

Blade internal loads: Fig. (5);

Blade displacements: Fig. (6).

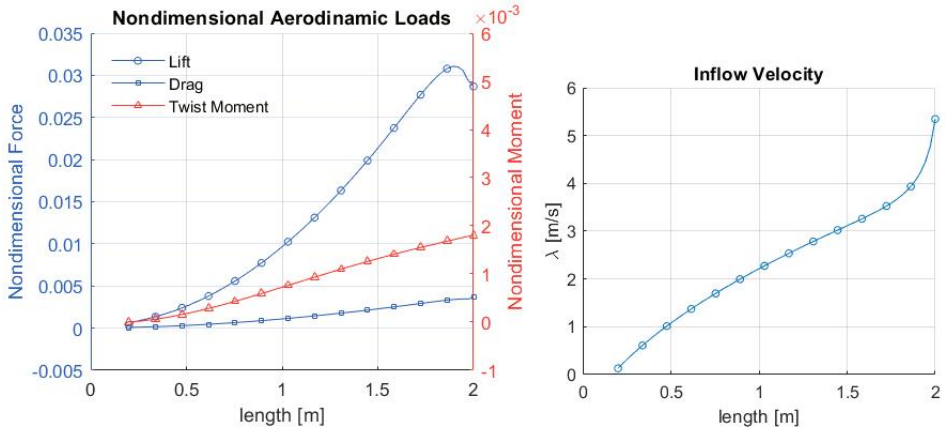

Figure 4: Nondimensionl Aerodynamic Loads and Inflow Velocity

In Fig. (4) , the dimensional inflow velocity represents the speed of the air mass that moves in the ground direction. The inflow has small values between the root and the center of the rotor, increasing as the length l increases and rising drastically at the tip, but it leads to a tip loss in lift.

In Fig. (5), the axial force F_1 is caused mainly by the centrifugal force field, produced by every blade's elements mass. Also, the shear force F_3 around the blade's root can be used in order to estimate the rotor's total lift, multiplying it by the number of blades. The observed total lift was approximately 120 N.

The linear displacements shown in Fig. (6) is used to analyse the structural integrity. Because of the material's low stiffness, the displacement u_3 is about 7.5% of the total length of the blade. The angular displacements are important because θ_1 can change the airfoil's angle of attack.

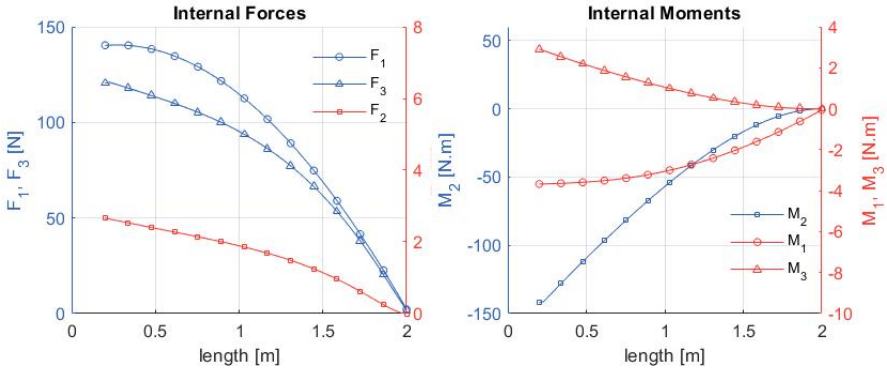

Figure 5: Blades's internal Forces and Moments

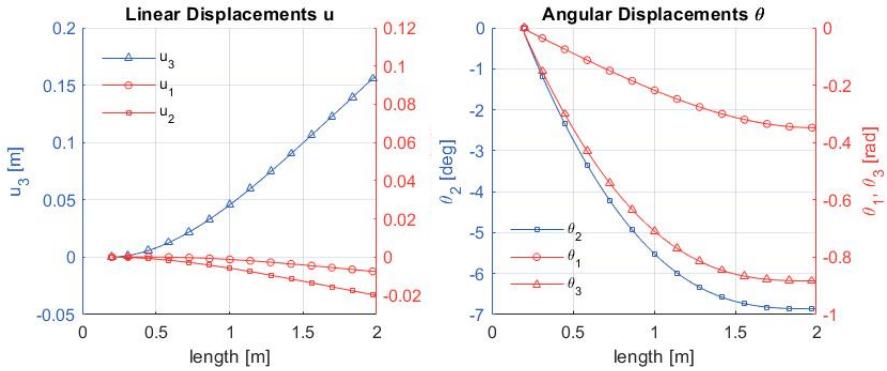

Figure 6: Blade's displacements

CONCLUSION

In this work, the aeroelastic model (structural and aerodynamic theories) was successfully integrated with the BEMT (inflow velocity computer). Because of the low computer effort, this type of analysis can be extremely efficiency in the early stages of a project, when the rotor's performances are compared. Different from Shang (1995), no symbolic variables were used which improved the computational efficiency in relation to his work

The rectangular blade built by the UH-60A was analysed and the results were consistent with the behavior of slender rotary blades undergoing aerodynamic loads. VABS showed that the cross-section has a low stiffness and the non-linearity of the internal forces would need to be considered to properly represent the displacements of the blade.

The tip loss of the lift started in about 95% of the length of the blade, which is a typical feature of rotor lift distribution. Also, the internal axial force caused by the rotation was observed as the highest force of the rotor in the simulated hover flight condition.

ACKNOWLEDGEMENTS

The authors thank FAPESP, Process. (2020/07335-1), for the financial research support.

REFERENCES

Andrade, D., 1992, "Application of Finite-State Inflow to Flap-Lag-Torsion Damping in Hover", Ph.D. thesis, Georgia Institute of Technology

Atilgan, A.R. and Hodges, D.H., 1991, "Unified Nonlinear Analysis for Non-homogeneous Anisotropic Beams with Closed Cross Sections". AIAA Journal, Vol. 29, No. 11, pp. 1990–1999.

Cesnik, C.E.S., 1994, "Cross-Sectional Analysis of Initially Twisted and Curved Composite Beams", Ph.D. thesis, Georgia Institute of Technology, Georgia.

Cheng, T., 2002, ”Structural Dynamic Modeling of Helicopter Blade for Computational Aeroelasticity”, Ph.D. thesis, Massachusetts Institute of Technology, Massachusetts.

Ghorashi, M., 2016, ”Statics and Rotational Dynamics of Composite Beams”. Springer International Publishing Switzerland, Gorham, ME.

Hodges, D.H., 1990, “A Mixed Variational Formulation Based on Exact Intrinsic Equations for Dynamics of Moving Beams”, Journal of Solids and Structures, Vol. 26, No. 11, pp. 1253–1273.

Hodges, D.H., 2006, ”Nonlinear composite beam theory”, Reston: AIAA, Atlanta, Georgia.

Hodges, D.H.; Ormiston, R. A., 1976, ”Stability of Elastic Bending and Torsion of Uniform Cantilever Rotor Blades in Hover With Variable Structural Coupling”, NASA Technical Note D-8192.

Shang, X., 1995, ”Aeroelastic Stability of Composite Hingeless Rotors with Finite-State Unsteady Aerodynamics”, Ph.D. thesis, Georgia Institute of Technology, Georgia.

Tian, S., Liu, X., Du, H., Tao, F. and Yu, W., 2021. ”iVABS Documentation”, https://wenbinyugroup.github.io/ivabs/index.html

RESPONSIBILITY NOTICE

The authors is are the only parties responsible for the printed material included in this paper.